GDCh
Research Articles
Angewandte Chemie International Edition
www.angewandte.org

How to cite: *Angew. Chem. Int. Ed.* **2024**, *63*, e202316360
doi.org/10.1002/anie.202316360

Li Superionic Conductors

Cubic Iodide Li_xYI_{3+x} Superionic Conductors through Defect Manipulation for All-Solid-State Li Batteries

*Shumin Zhang[+], Feipeng Zhao[+], Han Su[+], Yu Zhong, Jianwen Liang, Jiatang Chen, Matthew Liu Zheng, Jue Liu, Lo-Yueh Chang, Jiamin Fu, Sandamini H. Alahakoon, Yang Hu, Yu Liu, Yining Huang, Jiangping Tu, Tsun-Kong Sham, and Xueliang Sun**

Abstract: Halide solid electrolytes (SEs) have attracted significant attention due to their competitive ionic conductivity and good electrochemical stability. Among typical halide SEs (chlorides, bromides, and iodides), substantial efforts have been dedicated to chlorides or bromides, with iodide SEs receiving less attention. Nevertheless, compared with chlorides or bromides, iodides have both a softer Li sublattice and lower reduction limit, which enable iodides to possess potentially high ionic conductivity and intrinsic anti-reduction stability, respectively. Herein, we report a new series of iodide SEs: Li_xYI_{3+x} ($x=2$, 3, 4, or 9). Through synchrotron X-ray/neutron diffraction characterizations and theoretical calculations, we revealed that the Li_xYI_{3+x} SEs belong to the high-symmetry cubic structure, and can accommodate abundant vacancies. By manipulating the defects in the iodide structure, balanced Li-ion concentration and generated vacancies enables an optimized ionic conductivity of $1.04\times10^{-3}\,S\,cm^{-1}$ at 25 °C for Li_4YI_7. Additionally, the promising Li-metal compatibility of Li_4YI_7 is demonstrated via electrochemical characterizations (particularly all-solid-state Li-S batteries) combined with interface molecular dynamics simulations. Our study on iodide SEs provides deep insights into the relation between high-symmetry halide structures and ionic conduction, which can inspire future efforts to revitalize halide SEs.

Introduction

With the increasing popularity of electrical vehicles, all-solid-state lithium batteries (ASSLBs) are a promising choice to be the next-generation power source due to their intrinsic properties of high safety and high energy/powder density.[1] The key component of ASSLBs is the solid electrolyte (SE), whose advances have governed the development of ASSLBs.[2] SEs generally require a high ionic conductivity, good electrode compatibility, and decent mechanical properties for it to be considered an ideal electrolyte for high-performance ASSLBs.[1a,3] One of the most important evaluation factors for SEs is the ionic conductivity, which is closely correlated to the structure of SE materials.[4]

Lithium metal halide (Li-M-X)-based SEs have attracted extensive attention very recently, due to the breakthrough in achieving an ultra-high ionic conductivity of $10^{-2}\,S\,cm^{-1}$ level at room temperature (RT, 25 °C) that can be comparable to state-of-the-art sulfide SEs and liquid electrolytes

---

[*] S. Zhang,[+] F. Zhao,[+] H. Su,[+] J. Liang, M. L. Zheng, J. Fu, Y. Hu, Y. Liu, X. Sun
Department of Mechanical and Materials Engineering,
University of Western Ontario,
London, Ontario, N6A 5B9, Canada
E-mail: xsun9@uwo.ca

X. Sun
Eastern Institute for Advanced Study,
Eastern Institute of Technology,
Ningbo, Zhejiang 3150200, P. R. China

H. Su,[+] Y. Zhong, Y. Liu, J. Tu
State Key Laboratory of Silicon Materials, Key Laboratory of Advanced Materials and Applications for Batteries of Zhejiang Province, School of Materials Science & Engineering,
Zhejiang University
Hangzhou 310027, China

J. Chen
Cornell High Energy Synchrotron Source, Wilson Laboratory,
Cornell University
Ithaca, New York 14853, United States

J. Liu
Neutron Scattering Division,
Oak Ridge National Laboratory
Oak Ridge, TN 37831, United States

L.-Y. Chang
National Synchrotron Radiation Research Centre
101 Hsin-Ann Road, Hsinchu, 30076, Taiwan

S. H. Alahakoon, Y. Huang, T.-K. Sham
Department of Chemistry, University of Western Ontario
London, Ontario, N6A 5B7, Canada

[+] These authors contributed equally.

(LEs).[5] Most research about halide-based SEs focus on chlorides, as the high oxidation limit of chloride SEs (~4.3 V vs. Li^+/Li, the same hereafter) is regarded as suitable match for conventional oxide layered cathode materials.[6] Furthermore, the use of less-electronegative anions (Br^- and I^- comparing to Cl^-) sacrifices the oxidation stability.[7] As the experimental and calculated results indicated, the oxidation potential of bromides (~3.1 V) or iodides (~2.5 V) is distinctly lower than that of chlorides.[7b]

Yet theoretically, bromides or iodides show higher ionic conductivity compared to their chloride counterpart based on using the same M center element, because 1) the large-sized anions are relatively prone to realize a favorable anion stacking in the cubic close packing (*ccp*) for fast Li-ion migration.[6c] 2) The large polarizability of X (X = I shows the largest among Cl, Br, and I) results in the formation of soft Li-X sublattices, which present a loose interaction between Li and X, thus facilitating the Li-ion movement.[8] In addition, the reduction potential of Li-M-X is found to be associated with the polarizability of X in the constructed M-X sublattices, as M ions are relatively difficult to be chemically reduced when bonded to X with high polarizability.[7b,9] In this regard, developing iodide SEs has been recognized to improve the reduction stability of halide SEs, which is one of the major shortcomings of halide SEs in the cases of pairing with metal anodes (Li metal or alloys) to achieve high energy density ASSLBs.[6a,b,10] Moreover, the iodine-containing anode interphase is believed to play a positive role in extending the reduction potential when taking the kinetic contribution into consideration.[11]

The study of iodide SEs dates to the 1980s–1990s.[7a] The earliest studied $LiMI_4$ (M = Ga) and $LiMI_3$ (LiI-MI_2 solid solutions, M = Sc, Mn, Cd, Pb) were prepared by a melting method within ampoules.[12] They only showed high ionic conductivities (10^{-1}–10^{-2} S cm^{-1}) at a high temperature of ~300 °C. Reviving conventional halides (e.g., Li-In-Cl,[13] Li-Sc-Cl,[14] Li-Ho-Cl,[15] et al.) with high ionic conductivities (10^{-3} S cm^{-1} level) has initiated since the Panasonics employed mechanochemical ball-milling method to synthesize Li_3YCl_6 and Li_3YBr_6 SEs.[16] However, in this wave of reviving halide SEs, the exploration of iodide SEs are still limited to a simplex monoclinic crystal structure with low crystallographic symmetry and insufficient ionic conductivity at 10^{-4} S cm^{-1} level.[8,17]

In this work, we develop a series of Li_xYI_{3+x} (x = 2, 3, 4, or 9) via a ball-milling and post-annealing method. All the iodide SEs show high ionic conductivities of over 10^{-4} S cm^{-1}, and the highest value of 1.04 × 10^{-3} S cm^{-1} occurs at an optimal composition of Li_4YI_7 at RT. The long-range crystal structure of Li_xYI_{3+x} SEs are confirmed as the deficient NaCl-type cubic structure in the space group of *Fm-3m*. Local structures of Li_xYI_{3+x} were revealed to show that Y^{3+} partially replaces the Li^+ sites in the LiI and is coordinated with I^- to form YI_6^{3-} octahedra. Overall, the defects in the isotropic ion migration pathways of Li_4YI_7 are manipulated to improve ionic conductivity, which is demonstrated by the ab initio molecular dynamics (AIMD) simulations. Finally, the decent reduction stability of Li_4YI_7 is demonstrated by constructing Li-metal cells (symmetric cells and Li-S full cells) and interface molecular dynamics simulations, highlighting the unprecedented performance of iodide SEs.

Results and Discussion

LiI and YI_3 were used as the starting materials to synthesize a series of Li_xYI_{3+x} (x = 2, 3, 4, or 9), in which x is defined as the mole fraction value of LiI/YI_3. Y is proposed to partially replace the Li sites at each composition with different substitution percentages. As shown in Figure 1a, the X-ray diffraction (XRD) pattern of each Li_xYI_{3+x} (x = 2, 3, 4, or 9) SE can be well-indexed to a cubic LiI with a space group of *Fm-3m* (ICSD No. 04-016-5474). This indicates that the iodide framework exhibits an excellent structural inclusivity, while this feature cannot be extended to Y-based chlorides[18] or bromides (Figure S1). Furthermore, the diffraction peaks of each iodide SE gradually shift to a lower 2θ angle along with the decrease of x in Li_xYI_{3+x} (x = 2, 3, 4, or 9) as displayed in the magnified patterns (Figure S2). This distinct structural evolution corresponds to the gradually enlarged unit cell. More Y^{3+} is incorporated in the parent material of LiI, as Y^{3+} (90 pm) has a larger ionic radius compared to Li^+ (76 pm). It is expected that the Y substitution for Li in the structure of LiI expands the crystal lattice and promotes the Li-ion transport in Li_xYI_{3+x} (x = 2, 3, 4, or 9) SEs.

The ionic conductivities and activation energies (E_a) of Li_xYI_{3+x} (x = 2, 3, 4, or 9) SEs were evaluated by conducting temperature-dependent electrochemical impedance spectroscopy (EIS) measurements. Arrhenius plots of Li_xYI_{3+x} SEs based on temperature-dependent Nyquist plots (Figure S3) are plotted as exhibited in Figure S4. The general improvement of ionic conductivity is clearly indicated when different amounts of Y is introduced into the crystal structure of LiI. Corresponding E_a and ionic conductivity values (at RT) of Li_xYI_{3+x} SEs and LiI are shown in Figure 1b. At x = 9, when only a small amount of YI_3 (10 % mole ratio) is doped in the structure of LiI, E_a significantly drops from 0.41 eV (LiI) to 0.33 eV (Li_9YI_{12}), proving that Y substitution induces a larger 'bottleneck' size, which lowers the activation barriers for Li-ion diffusion. As a result, Li_9YI_{12} shows an enhanced conductivity of 1.16×10^{-4} S cm^{-1}, which is a three-order-of-magnitude improvement compared to the pristine LiI (10^{-7} S cm^{-1} level). When further increasing the Y substitution percentage (corresponding to a decreased x value), the highest ionic conductivity of 1.04×10^{-3} S cm^{-1} was achieved for the Li_4YI_7 (x = 4), corresponding to the lowest activation energy of 0.26 eV. Ab initio molecular dynamics (AIMD) simulated that the activation energy of Li-ion migration in Li_4YI_7 was 0.28 eV (Figure S5), which agreed well with the experimental value. The electronic conductivity of Li_4YI_7 SE was determined as 2.09×10^{-7} S cm^{-1} through conducting direct current (DC) polarization measurements (Figure S6). The electronic conductivity of Li_4YI_7 is located at a relatively higher level compared to most reported SEs (10^{-7}–10^{-9} S cm^{-1}),[19] but considering the value is still four-orders-of-magnitude lower than the ionic conductivity,

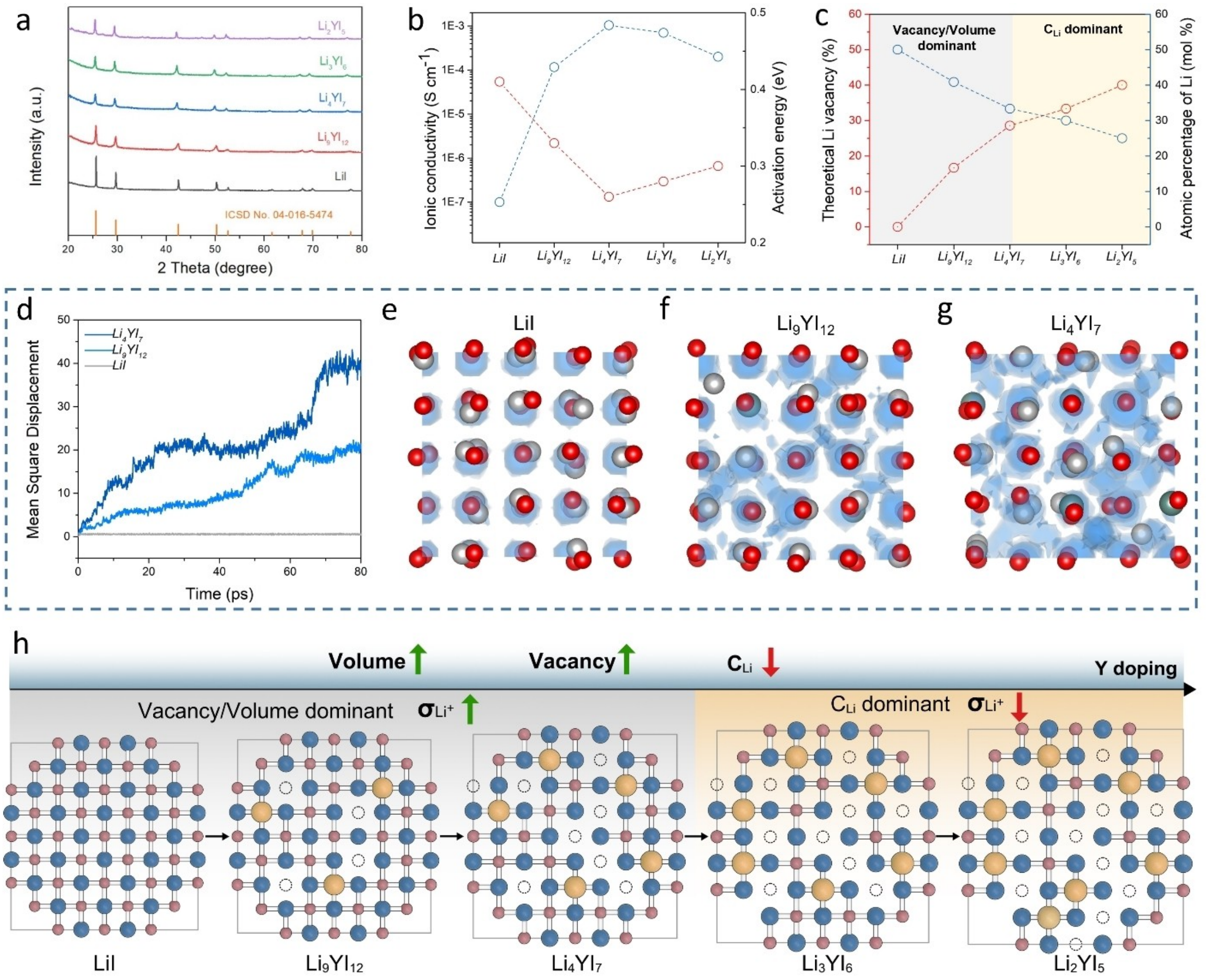

Figure 1. (a) Lab-based XRD patterns of the prepared Li_xYI_{3+x} ($x=2$, 3, 4, or 9) SEs. (b) The trend of change of the ionic conductivities (at RT) and activation energies of Li_xYI_{3+x} ($x=2$, 3, 4, or 9) SEs and LiI. (c) Evolution of the generated vacancies and the corresponding Li concentration for the series of Li_xYI_{3+x} ($x=2$, 3, 4, or 9) SEs and LiI. (d) Profiles of the Mean Square Displacement (MSD) values for LiI, Li_9YI_{12}, and Li_4YI_7 at 600 K. Trajectories (Blue) of Li atoms (Grey) for (e) LiI, (f) Li_9YI_{12}, and (g) Li_4YI_7 in ab initio MD simulations at 600 K. Y atoms in dark green color and I atoms in red color. (h) A Scheme of the trade-off principle between Li vacancy and concentration toward an optimized ionic conduction for Li_xYI_{3+x} ($x=2$, 3, 4, or 9) SEs.

which it appears the Li_4YI_7 is sufficient in supporting effective ionic conduction while insulating electrons.

Based on the principle of substitutional effects, it is believed that the introduction of one Y^{3+} ion into the crystal lattice of LiI can effectively substitute three Li^+ cations, thereby inducing the formation of two intrinsic vacancies (V’). Notably, as with the increase of Y^{3+} content, there is a corresponding rise in the concentration of V’ while an equivalent number of Li ions are excluded to maintain charge balance (Figure 1c). Furthermore, as XRD results indicate, the substitution of Y^{3+} leads to an expansion of the unit cell volume. Therefore, we propose that both the creation of V’ and the simultaneous expansion of the unit cell can provide an open spatial environment which facilitates the easy movement of Li ions. To confirm this hypothesis, we performed AIMD simulations on LiI, Li_9YI_{12}, and Li_4YI_7 at a high temperature of 600 K. Analysis of the mean square displacement (MSD) profiles shows a close connection between the kinetics of Li-ion diffusion and the doping concentration of Y (Figure 1d). Furthermore, a comparative analysis of the trajectories of Li ions in LiI, Li_9YI_{12}, and Li_4YI_7 (Figure 1e–g) at a probability density of $2P_0$ and the corresponding 3D Li-ion migration pathways (Figure S7), reveals that the localized Li^+ mobility inherent to LiI becomes delocalized with the introduction of sites devoid of Li occupancy and the expansion of the unit cell. However, it is important to note that the ionic conductivity of Li-Y-I SEs is not solely determined by cell volume and vacancy concentration. Li_3YI_6 ($x=3$) and Li_2YI_5 ($x=2$) exhibit higher levels of Y substitution and larger unit cell parameters compared to Li_4YI_7, while they display lower ionic conductivities of 7.0×10^{-4} S cm^{-1} and 2.0×10^{-4} S cm^{-1}, respectively (Figure 1b). Despite the incorporation of additional Y enlarges the unit cell and creates more V’, it results in a reduction of the charge carrier (Li ions) concentration. As a result, there is a trade-off between the created V’ and eliminated Li ions leading to optimized ionic conduction property. (Figure 1h). In addition, taking the advantage of the structural inclusivity of iodide, we can incorporate hetero anions into the structure to further improve the ionic conductivity through increasing site disorders as reported in Li Argyrodites.[20] As shown in Figure S8, the flexible compositional manipulation has been realized in $Li_4YI_{7-x}Br_x$ ($x=0$, 1, 2, 3, 3.5) SEs with an identical "LiI" structure. The intrinsic I^-/Br^- anion site disorder leading to an optimized ionic conductivity up to 1.49×10^{-3} S cm^{-1} for the composition of $Li_4YI_{3.5}Br_{3.5}$ (Figure S9).

With regard for the representative Li_9YI_{12} and Li_4YI_7, we first employed Rietveld refinement on synchrotron-based high-resolution powder X-ray diffraction (SXRD) patterns to analyze their detailed crystal structures. As shown in Figure 2a and b, the refined SXRD patterns for Li_9YI_{12} and Li_4YI_7 are reasonable with low observation-calculation differences (Rwp $_{Li9YI12}$: 2.887 %, Rwp $_{Li4YI7}$: 1.958 %). Detailed structural and Rietveld refinement information are shown in Table S1–S4. We further employed time-of-fight neutron powder diffraction (TOF-NPD) to analyze the coordinate and occupancy of each atoms, as this technique is more sensitive than X-ray diffraction and enable us to detect lighter element (e.g., Li).[21] Via joint Rietveld refinement for the SXRD and NPD data, we improved the accuracy of solved crystal structure of Li_9YI_{12} and Li_4YI_7. As summarized in Table S5–S7, the Li vacancies in Li_9YI_{12} and Li_4YI_7 SEs are 15.91 % and 28.29 %, respectively, which are very close to their theoretical value (16.67 % and 28.57 %). We extracted the refined NPD data from the joint refinement process as exhibited in Figure 2c and d. The excellent goodness-of-fit (GOF) was obtained for each case. Therefore, it was confirmed that the crystal structure of the representative Li_9YI_{12} and Li_4YI_7 materials that we initially solved via refining SXRD data is highly plausible. The resultant crystal structures of Li_9YI_{12} and Li_4YI_7 are schematically illustrated in Figure 2e and f, respectively. There are only two Wyckoff sites: one is 4a, and the other one is 4b, in which I^- ions at 4b sites are cubic-close-packed to form octahedral voids. Li^+, Y^{3+}, and V' are co-occupied at 4a sites. Different from the recently predicted (i.e., Li_3LaI_6 and Li_3YI_6)[17a] and experimentally verified (i.e., Li_3HoI_6 and Li_3ErI_6)[8,17c] monoclinic structure of iodide SEs, our Li_xYI_{3+x} SEs show a highly symmetric sublattice that can be regarded as deficient NaCl-type structure. Such a structure has high similarities with the predicted Suzuki phase $6NaCl{\cdot}CdCl_2$, while the difference is that in $6NaCl{\cdot}CdCl_2$, there are separate positions for Na^+ (face center), Cd^{2+} (corners) and vacancies (corners).[22] To reiterate the accuracy of our determined crystal structure (cubic, *Fm-3m*) for Li_xYI_{3+x} with high symmetry, we conducted a reverse verification by assigning the structure of synthesized Li_9YI_{12} and Li_4YI_7 materials to a monoclinic phase (space group of *C2/c* or *C2*).[17a] As shown in Figure S10, we refined the SXRD data under the frame of monoclinic structure, but the resultant refinement quality (R value and the visual assessment of the profile differences) is relatively poor, indicating that monoclinic structure is not acceptable for our Li_xYI_{3+x} SEs. Furthermore, we also carried out Rietveld refinements for the neutron data of Li_3YI_6 and Li_2YI_5 materials based on the cubic LiI structure, as exhibited in Figure S11. The refined cell parameters (*a*

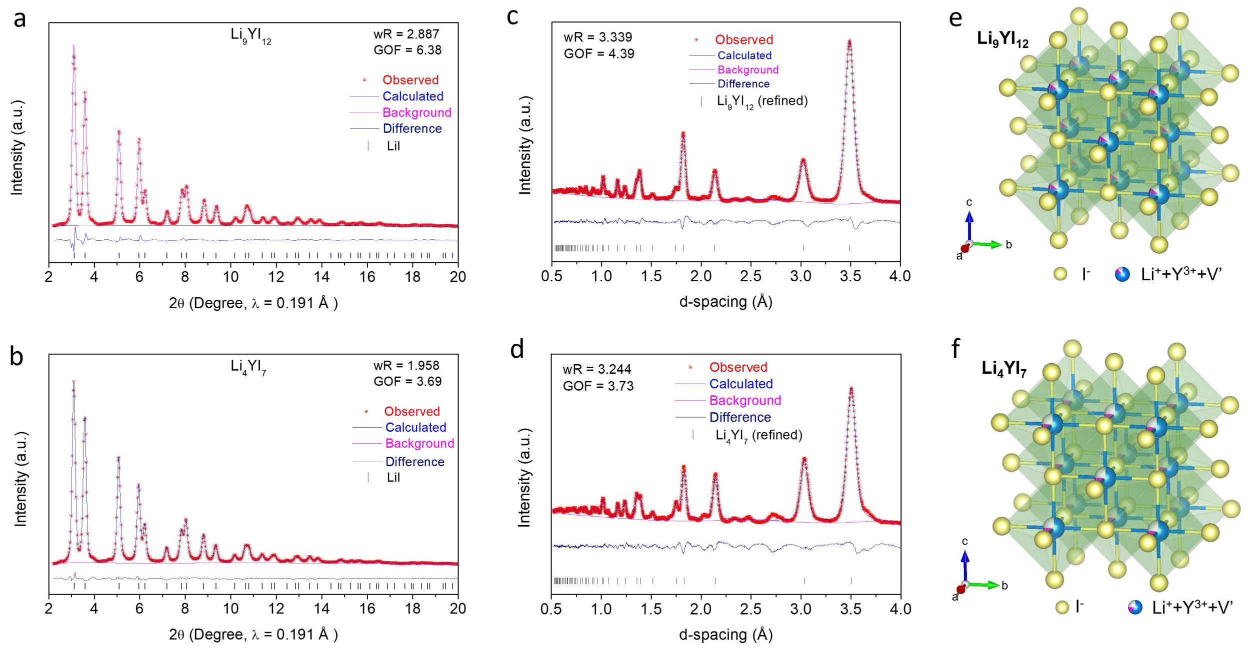

Figure 2. (a, b) Rietveld refinement for the SXRD pattern for Li_9YI_{12} and Li_4YI_7, respectively. The experimental profile is shown in red crosses; the blue line denotes the calculated pattern; the difference of profile is shown in navy; positions of the Bragg reflections is based on the referred LiI. (c, d) Refinement results for the TOF-NPD data of Li_9YI_{12} and Li_4YI_7, respectively, extracted from the joint synchrotron-neutron Rietveld refinement process. (e, f) Crystal structures of Li_9YI_{12} and Li_4YI_7, respectively.

and cell volume) of the series of Li$_x$YI$_{3+x}$ SEs ($x=2$, 3, 6, 9) are extracted and plotted in Figure S12. The upward trends in both *a* value and cell volume gradually decelerate as increasing Y substitution incorporated in the structure of LiI, indicating the $x=2$ (Li$_2$YI$_5$) is very close to the solid solution limit.

The local structure of the prepared Li$_x$YI$_{3+x}$ SEs was further studied via the analysis of the synchrotron-based X-ray characterizations. Figure 3a compares X-ray absorption near edge spectra (XANES) of I L_3-edge of Li$_x$YI$_{3+x}$ ($x=3$, 4, and 9) SEs and LiI. The "white line" peak at 4562.9 eV is calculated to correspond to the dipole transition from I 2$p_{3/2}$ to I 5*s* orbital hybridized with Li 2*s* orbitals (Figure S13). The reduced peak intensity is relative to x decreasing, which suggests the formation of more Li vacancies at the octahedral sites in LiI, thus validating our discussion on the generation of Li vacancies with different Y doping percentage in the structure of Li$_x$YI$_{3+x}$ ($x=3$, 4, or 9) SEs. Then, X-ray total scattering for the representative Li$_9$YI$_{12}$ and Li$_4$YI$_7$ SEs was studied. The pair distribution function (PDF) $G(r)$ along with the PDF fitting results for Li$_9$YI$_{12}$ and Li$_4$YI$_7$ are shown in Figure 3b. The PDF-fitted patterns within the *r* range of 2–20 Å show little differences ($R_{\mathrm{wLi9YI12}}=0.074$, $R_{\mathrm{wLi4YI7}}=0.083$) compared to the experimental result, which further proves the refined crystal structure from X-ray diffraction and Neutron diffraction is accurate. For both spectra, the first reasonable peak corresponding to molecular bonds is located at 3.034 Å, which can be assigned to the contribution from Y(Li)-I bonding based on the single-scattering information from wavelet-transformed (WT) EXAFS results (Figure 3c). This distance is longer than interatomic distance of Li-I (3.013 Å) performed in the structure of the referred LiI material, further reiterating that partially replacing Li with Y induces to expand the unit cell. The second peak at 4.307 Å shows narrow width with high symmetry, which is attributed to the nearest I-I or Y(Li)-Y(Li) atomic pairs. Notably, in Li$_4$YI$_7$ data profiles, the fitted curve was well-matched with experimental data within a unit cell range (data before 6.07 Å), indicating that vacancies, Li, and Y atoms uniformly share the same 4a Wycoff site. Last, XANES and extended X-ray absorption fine structure (EXAFS) of Y *K*-edge were analyzed to deliver quantitative structure information of the Li$_4$YI$_7$ SEs (Figure S14). Phase-uncorrected radial distribution functions (RDF) after Fourier Transformed (FT) EXAFS for Li$_4$YI$_7$ is fitted as exhibited in Figure 3d. Intensive signals caused by iodine signal scattering can be found at 2.6 Å. Y-I coordination is fitted at the bonding distance of 3.016 Å with a coordination number of 6.5 (Table S8), which is close to the model we proposed. The Li site in Li$_4$YI$_7$ was also identified by ^{6}Li magic angle spinning nuclear magnetic resonance (^{6}Li MAS NMR), which is a sensitive technique to the atomic and electronic environment of Li element.[23] As displayed in Figure 3e, a distinct ^{6}Li NMR peak is observed at −3.9 ppm in the Li$_4$YI$_7$ sample. In contrast to the sharp ^{6}Li resonance at −4.6 ppm in the reference LiI sample, the signal from

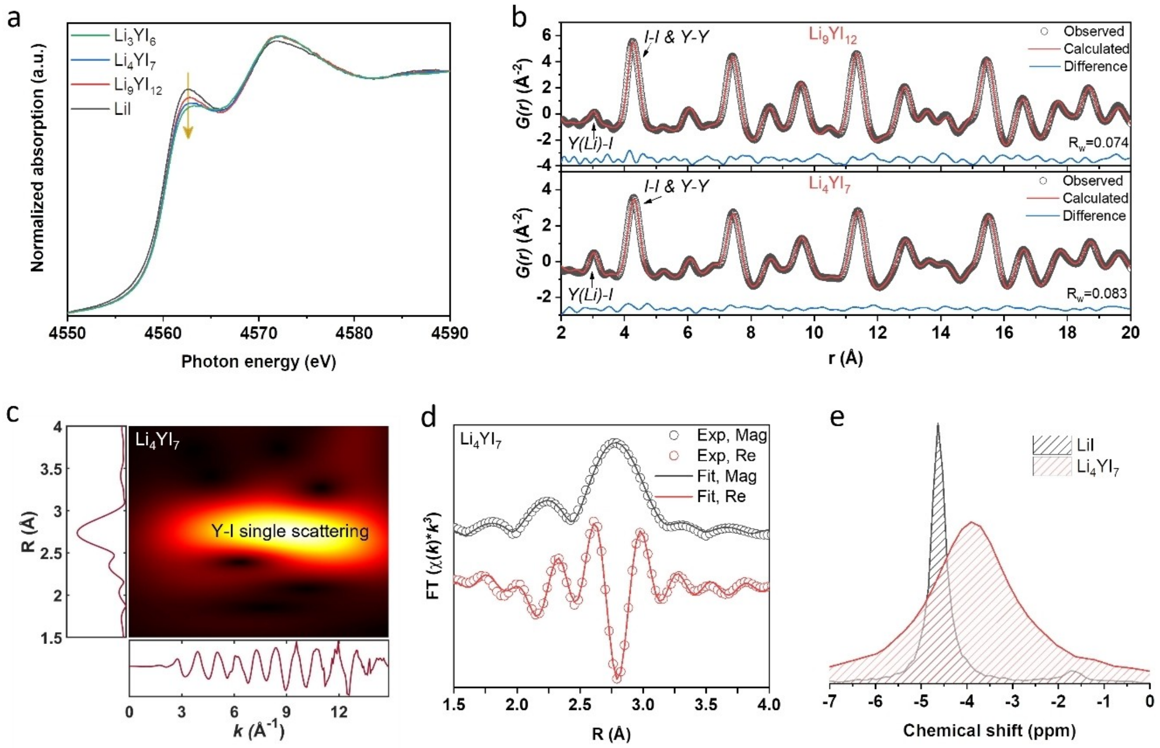

Figure 3. (a) I L_3-edge XANES spectra of the Li$_x$YI$_{3+x}$ ($x=3$, 4, or 9) SEs compared with LiI. (b) Pair distribution function $G(r)$ and fitting results for Li$_9$YI$_{12}$ and Li$_4$YI$_7$. (c) WT spectrum of Li$_4$YI$_7$. (d) Fitting results of the k^3-weighted FT spectra of Li$_4$YI$_7$ at Y *K*-edge, showing the experimental data (grey circle) and Feff modeling (grey line) in terms of magnitude of FT and the real part of FT experimental data (red circle) and Feff modeling (red line) traces. The R factor for this fitting is 0.003 and S_0^2 is set as 0.81. (e) ^{6}Li MAS NMR spectra of Li$_4$YI$_7$ and LiI.

Li_4YI_7 exhibits a broad Gaussian lineshape, suggesting a disordered Li local environment. This broadening of the signal is attributed to the presence of varied Li local structures arising from the substitution of Y.

Although the oxidation limit of Li-Y-I SEs was inherently restricted by the oxidation of I^- to I_2 at approximately 3.4 V vs. Li^+/Li, the cathodic stability of the Li_4YI_7 SE was decent and only with minimal reduction current in our CV measurements (Figure S15). Thermodynamic calculations indicated that Li_4YI_7 shows less reactivity with Li metal, as well as lower reduction potential compared with Li_3YCl_6 and Li_3YBr_6 (Figure S16). This agrees well the previously reported results about the superiority of iodide SEs in the aspect of reduction stability compared with the chloride and bromide counterparts.[9] The reduction stability of Li_4YI_7 SEs was experimentally evaluated by testing the performance of Li‖Li_4YI_7‖Li symmetric cells. The evolution of the Li/Li_4YI_7 interfacial impedance was examined by recording the interval Nyquist plots upon resting at the state of open circuit voltage (OCV). As shown in Figure S17, through fitting for the Nyquist plots, we identified the negligible resistance change for both the bulk Li_4YI_7 SE and anode/Li_4YI_7 total interface.[24] Therefore, the spontaneous formation of chemically stabilized interface between Li_4YI_7 and Li metal was proved. With the help of the stabilized interphase, highly stable plating/stripping was realized in the Li‖Li_4YI_7‖Li symmetric cells under various current densities and cut-off capacities (Figure S18). For comparison, we also employed a representative halide electrolyte involving Y, namely Li_3YCl_6 (LYC) to observe a trend of polarization escalation and soft break down in a short time, manifesting the inherent instability of this electrolyte in the presence of lithium metal.

Concomitantly, we undertook the development of theoretical interface models for both the Li/LYC and Li/Li_4YI_7 configurations by AIMD simulations conducted at an elevated temperature of 400 K. By analyzing the snapshots acquired before and after these simulations, it is revealed that Y species within the LYC electrolyte undergo reduction and infiltrate the adjacent lithium layer, resulting in the formation of a Li-Y alloy, as illustrated in Figure 4a. Moreover, corroboration of this transformative process is also illustrated in the corresponding outcomes of the radical distribution function (RDF), where the distinctive peak corresponding to YCl_6 octahedra at the distance of 2.5 Å undergoes disintegration throughout the course of the simulation, as shown in Figure 4b and 4c. Further insights can be collected from the Li-Y pair results, which indicate the emergence of a Li-Y alloy characterized by shortened bond lengths. It is noteworthy that this alloy-rich interfacial layer exhibits a discernible degree of electronic conductivity, thereby promoting the continuous deterioration of the electrolyte. Conversely, the outcomes stemming from the interface simulations involving Li/Li_4YI_7, as elucidated in Figure 4d-f, serve as proofs to the marked enhancement in stability at the interface of Li_4YI_7 and Li anode. Both the snapshots and the indicative RDF profiles pertaining to the Li-Y and Y-I pairs do not indicate any obvious decomposition of the YI_6 octahedral, nor do they attest to the formation of a Li-Y alloy after the simulations.

XPS measurements were also conducted to prove the stabilized Li/Li_4YI_7 interface (Figure S19). The Li 1s spectrum was located at the binding energy of ~55.6 eV, which showed a considerable deviation to the binding energy of metallic Li (below 55 eV), indicating that Li dendrites was excluded at the interface. Typical and well-defined 3d spectra were maintained for Y and I elements, indicating that no additional contributions from heterogeneous compositions were found. In this regard, we were able to fabricate all-solid-state Li-S batteries (ASSLSBs) by using Li_4YI_7 SE directly paired with a Li metal anode. As displayed in Figure 4g, the constructed Li_4YI_7-based ASSLSBs operated well at a current density of 0.127 mA cm^{-2} and 25 °C, delivering a reversible capacity of 1193 mAh g^{-1} in the third charge/discharge process. A single charge/discharge plateau appeared to show a typical conversion between S and discharged products (mixture of Li_2S_2 and Li_2S) in ASSLSBs.[25] However, the Coulombic efficiency of the cell increased with increasing cycle number (Figure S20), suggesting the Li dendrites might be still growing under the circumstance of long cycling. The issue of Li dendrite penetration, even for a chemically stabilized Li/SE interface, has been gradually regarded as an engineering problem.[26] It is heavily dependent on developing an unique electrode architecture to alleviate this issue,[27] which is unfortunately out of scope of the presented research. Even so, we still demonstrated the application of Li_4YI_7 by replacing the Li metal with LiIn alloy for achieving high-performance ASSLSBs (Figure 4h). It is worth noting that the Li_4YI_7 was not only used as the single SE layer to construct our ASSLSBs, but also it served as an effective additive to prepare the S cathode composite. As we all know, the iodide (i.e., LiI) has been reported as an additive to boost the redox reaction in ASSLSB,[28] the highly ionic conductive Li_4YI_7 (4 order-of-magnitude higher than LiI) is believed to play a more important role to facilitate Li-ion exchange in the redox reaction of S cathode materials. The full cell showed poor cycling reversibility if without the Li_4YI_7 additive in the S cathode composite (Figure S21). It is suggested to further study the working mechanism of highly conductive iodide SEs for ASSLSBs in detail.

Conclusion

In summary, we manipulated the defects in the series of Li_xYI_{3+x} (x=2, 3, 4, or 9) SEs with high-symmetric cubic crystal structure and promising ionic conductivities up to 1.04×10^{-3} S cm^{-1} at room temperature. The high ionic conductivity attributable to the crystal structure that has been thoroughly studied by joint Rietveld refinement for the synchrotron XRD and NPD data, as well as XAS and PDF analyses. The obtained Li_xYI_{3+x} SE materials can be regarded as partially incorporating Y into the structure of LiI. Upon Y incorporation, the trade-off between the generated defects of Li vacancies and the Li concentration plays a crucial role in delivering an optimized ionic

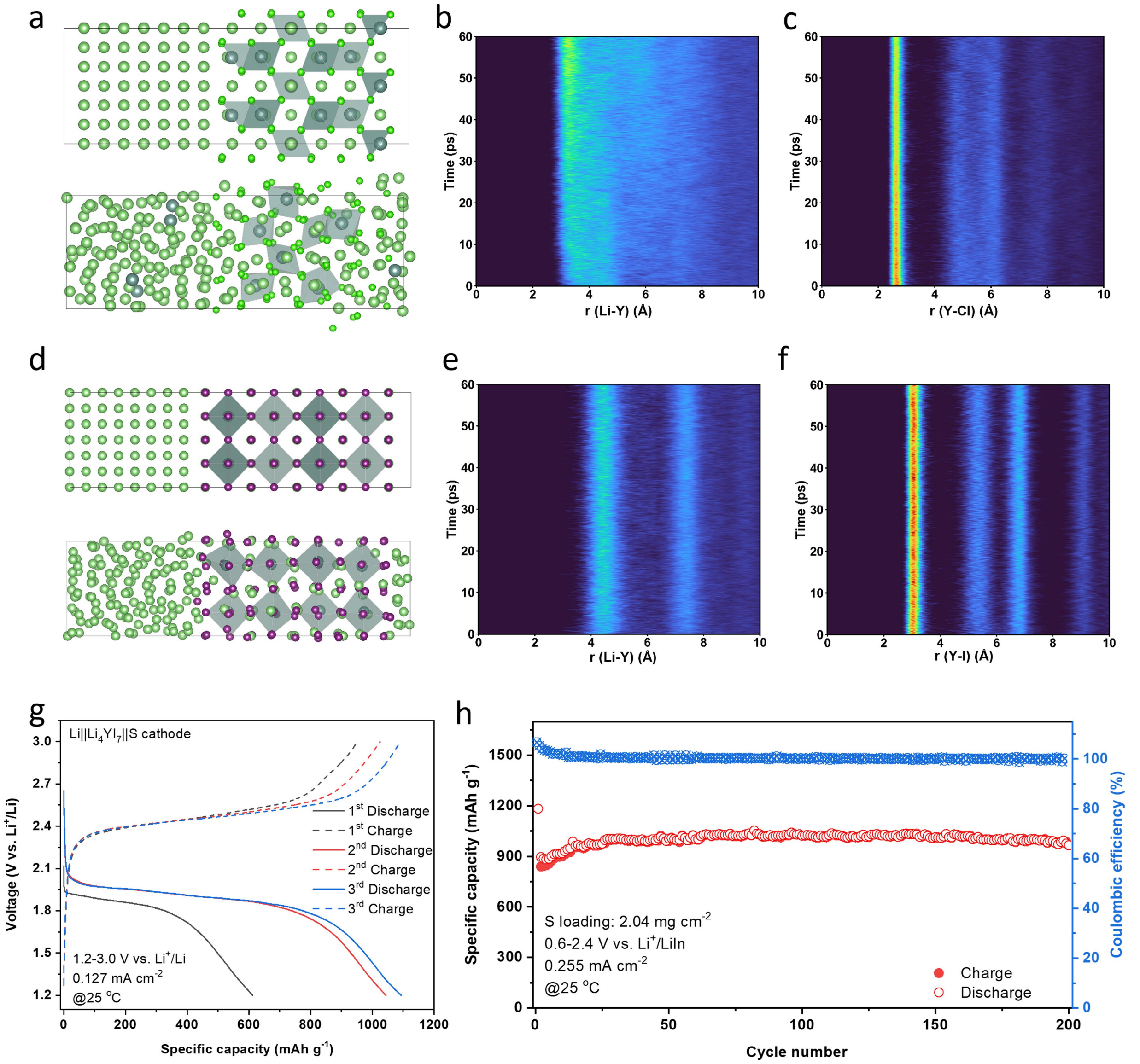

Figure 4. (a) Snapshots of Li/LYC interface before and after AIMD simulations at 400 K, and the corresponding radial distribution function of (b) Li-Y pair and (c) Y-Cl pair. (d) Snapshots of Li/Li_4YI_7 interface before and after AIMD simulations at 400 K, and the corresponding radial distribution function of (e) Li-Y pair and (f) Y-I pair. (g) Charge-discharge curves of the Li||Li_4YI_7||S ASSLSB. (h) Long-term cycling performance of the LiIn||Li_4YI_7||S ASSLSB.

conductivity for the composition of Li_4YI_7 ($x=4$ for the Li_xYI_{3+x}). This principle has also been verified by conducting AIMD simulations for the typical Li_xYI_{3+x} materials. In addition, the Li-metal compatibility of the Li_4YI_7 SE was demonstrated by constructing long-cycling Li-metal symmetric cells and Li-S full cells, as well as carrying out dedicate Li metal/SE interface molecular dynamics simulations (comparing to those of the representative Li_3YCl_6). Our work on the exploration of new iodide SEs represents a new research direction, offering deep insights into the structural manipulation towards superionic conductors and applications of halide SEs with excellent Li-metal compatibility.

Author contributions

S.Z., F.Z., and X.S. conceived and designed the experiments. S.Z. and F.Z. prepared samples and carried out the main experiments. S.Z., L.C., J.F., Y.H., and T.K.S. performed synchrotron data acquisition, analyses and discussion. F.Z. and J.L. solved the crystal structure. H.S., Y.Z., Y.L., and J.T. carried out the simulations. F.Z., S.A., and Y.H. conducted NMR characterizations. S.Z., F.Z., and H.S. wrote the original manuscript. M.Z. edited the manuscript. All authors commented the manuscript. X.S. supervised the whole project.

Acknowledgements

This research was supported by the Natural Sciences and Engineering Research Council of Canada (NSERC), the Canada Research Chair Program (CRC), the Canada Foundation for Innovation (CFI), Ontario Research Foundation (ORF), and the University of Western Ontario (UWO). The synchrotron research was performed at the Canadian Light Source, a national research facility of the University of Saskatchewan, which was supported by the CFI, NSERC, the National Research Council (NRC), the Canadian Institutes of Health Research (CIHR), the Government of Saskatchewan, and the University of Saskatchewan. A portion of this research used resources (NOMAD) at the Spallation Neutron Source, a DOE Office of Science User Facility Operated by the Oak Ridge National Laboratory. We thank Prof. Hong Zhu from Shanghai Jiao Tong University for providing the crystallographic information files of non-cubic Li_3YI_6.

Conflict of Interest

The authors declare no conflict of interest.

Data Availability Statement

The data that support the findings of this study are available from the corresponding author upon reasonable request.

Keywords: solid electrolytes · iodides · ionic conductivity · reduction stability · cubic crystal structures

---

[1] a) J. Janek, W. G. Zeier, *Nat. Energy* **2023**, *8*, 230–240; b) Y.-K. Sun, *ACS Energy Lett.* **2020**, *5*, 3221–3223; c) X. Q. Zeng, M. Li, D. Abd El-Hady, W. Alshitari, A. S. Al-Bogami, J. Lu, K. Amine, *Adv. Energy Mater.* **2019**, *9*, 1900161.

[2] a) X. Y. Feng, H. Fang, N. Wu, P. C. Liu, P. Jena, J. Nanda, D. Mitlin, *Joule* **2022**, *6*, 543–587; b) Q. Zhao, S. Stalin, C.-Z. Zhao, L. A. Archer, *Nat. Rev. Mater.* **2020**, *5*, 229–252; c) R. Chen, Q. Li, X. Yu, L. Chen, H. Li, *Chem. Rev.* **2019**, *120*, 6820–6877; d) W. Zhao, J. Yi, P. He, H. Zhou, *Electrochem. Energy Rev.* **2019**, *2*, 574–605.

[3] a) A. Manthiram, X. Yu, S. Wang, *Nat. Rev. Mater.* **2017**, *2*, 16103; b) M. Weiss, F. J. Simon, M. R. Busche, T. Nakamura, D. Schröder, F. H. Richter, J. Janek, *Electrochem. Energy Rev.* **2020**, *3*, 221–238.

[4] a) Y. Li, S. Song, H. Kim, K. Nomoto, H. Kim, X. Sun, S. Hori, K. Suzuki, N. Matsui, M. Hirayama, T. Mizoguchi, T. Saito, T. Kamiyama, R. Kanno, *Science* **2023**, *381*, 50–53; b) S. Ohno, A. Banik, G. F. Dewald, M. A. Kraft, T. Krauskopf, N. Minafra, P. Till, M. Weiss, W. G. Zeier, *Prog. Energy* **2020**, *2*, 022001.

[5] a) Y. Tanaka, K. Ueno, K. Mizuno, K. Takeuchi, T. Asano, A. Sakai, *Angew. Chem. Int. Ed.* **2023**, *62*, e202217581; b) Y. Ishiguro, K. Ueno, S. Nishimura, G. Iida, Y. Igarashib, *Chem. Lett.* **2023**, *52*, 237–241; c) S. Zhang, F. Zhao, J. Chen, J. Fu, J. Luo, S. H. Alahakoon, L.-Y. Chang, R. Feng, M. Shakouri, J. Liang, Y. Zhao, X. Li, L. He, Y. Huang, T.-K. Sham, X. Sun, *Nat. Commun.* **2023**, *14*, 3780.

[6] a) C. Wang, J. Liang, J. T. Kim, X. Sun, *Sci. Adv.* **2022**, *8*, eadc9516; b) H. Kwak, S. Wang, J. Park, Y. S. Liu, K. T. Kim, Y. Choi, Y. F. Mo, Y. S. Jung, *ACS Energy Lett.* **2022**, *7*, 1776–1805; c) J. W. Liang, X. N. Li, K. R. Adair, X. L. Sun, *Acc. Chem. Res.* **2021**, *54*, 1023–1033.

[7] a) X. N. Li, J. W. Liang, X. F. Yang, K. R. Adair, C. H. Wang, F. P. Zhao, X. L. Sun, *Energy Environ. Sci.* **2020**, *13*, 1429–1461; b) S. Wang, Q. Bai, A. M. Nolan, Y. S. Liu, S. Gong, Q. Sun, Y. F. Mo, *Angew. Chem. Int. Ed.* **2019**, *58*, 8039–8043.

[8] R. Schlem, T. Bernges, C. Li, M. A. Kraft, N. Minafra, W. G. Zeier, *ACS Appl. Energ. Mater.* **2020**, *3*, 3684–3691.

[9] K. Kim, D. Park, H. G. Jung, K. Y. Chung, J. H. Shim, B. C. Wood, S. Yu, *Chem. Mater.* **2021**, *33*, 3669–3677.

[10] Y.-C. Yin, J.-T. Yang, J.-D. Luo, G.-X. Lu, Z. Huang, J.-P. Wang, P. Li, F. Li, Y.-C. Wu, T. Tian, Y.-F. Meng, H.-S. Mo, Y.-H. Song, J.-N. Yang, L.-Z. Feng, T. Ma, W. Wen, K. Gong, L.-J. Wang, H.-X. Ju, Y. Xiao, Z. Li, X. Tao, H.-B. Yao, *Nature* **2023**, *616*, 77–83.

[11] a) Y. Zhu, X. He, Y. Mo, *ACS Appl. Mater. Interfaces* **2015**, *7*, 23685–23693; b) F. Zhao, J. Liang, C. Yu, Q. Sun, X. Li, K. Adair, C. Wang, Y. Zhao, S. Zhang, W. Li, S. Deng, R. Li, Y. Huang, H. Huang, L. Zhang, S. Zhao, S. Lu, X. Sun, *Adv. Energy Mater.* **2020**, *10*, 1903422; c) E. Umeshbabu, B. Zheng, Y. Yang, *Electrochem. Energy Rev.* **2019**, *2*, 199–230; d) O. Sheng, C. Jin, Z. Ju, J. Zheng, T. Liu, Y. Liu, Y. Wang, J. Luo, X. Tao, J. Nai, *Nano Lett.* **2022**, *22*, 8346–8354.

[12] a) W. Hönle, B. Hettich, A. Simon, *Zeitschrift für Naturforschung B* **1987**, *42*, 248–250; b) A. Lachgar, D. S. Dudis, P. K. Dorhout, J. D. Corbett, *Inorg. Chem.* **1991**, *30*, 3321–3326; c) H. D. Lutz, Z. Zhang, A. Pfitzner, *Solid State Ionics* **1993**, *62*, 1–3.

[13] X. N. Li, J. W. Liang, J. Luo, M. N. Banis, C. H. Wang, W. H. Li, S. X. Deng, C. Yu, F. P. Zhao, Y. F. Hu, T. K. Sham, L. Zhang, S. Q. Zhao, S. G. Lu, H. Huang, R. Y. Li, K. R. Adair, X. L. Sun, *Energy Environ. Sci.* **2019**, *12*, 2665–2671.

[14] a) J. W. Liang, X. N. Li, S. Wang, K. R. Adair, W. H. Li, Y. Zhao, C. H. Wang, Y. F. Hu, L. Zhang, S. Q. Zhao, S. G. Lu, H. Huang, R. Y. Li, Y. F. Mo, X. L. Sun, *J. Am. Chem. Soc.* **2020**, *142*, 7012–7022; b) L. D. Zhou, C. Y. Kwok, A. Shyamsunder, Q. Zhang, X. H. Wu, L. F. Nazar, *Energy Environ. Sci.* **2020**, *13*, 2056–2063.

[15] J. W. Liang, E. van der Maas, J. Luo, X. N. Li, N. Chen, K. R. Adair, W. H. Li, J. J. Li, Y. F. Hu, J. Liu, L. Zhang, S. Q. Zhao, S. G. Lu, J. T. Wang, H. Huang, W. X. Zhao, S. Parnell, R. I. Smith, S. Ganapathy, M. Wagemaker, X. L. Sun, *Adv. Energy Mater.* **2022**, *12*, 2103921.

[16] T. Asano, A. Sakai, S. Ouchi, M. Sakaida, A. Miyazaki, S. Hasegawa, *Adv. Mater.* **2018**, *30*, 1803075.

[17] a) Z. M. Xu, X. Chen, K. Liu, R. H. Chen, X. Q. Zeng, H. Zhu, *Chem. Mater.* **2019**, *31*, 7425–7433; b) N. Flores-Gonzalez, N. Minafra, G. Dewald, H. Reardon, R. I. Smith, S. Adams, W. G. Zeier, D. H. Gregory, *ACS Materials Lett.* **2021**, *3*, 652–657; c) M. A. Plass, S. Bette, R. E. Dinnebier, B. V. Lotsch, *Chem. Mater.* **2022**, *34*, 3227–3235.

[18] a) T. Yu, L. Wang, Q. Sun, B. Xiao, X. Bai, R. Yang, Y. Duan, Y. Wu, G. Li, G. Xu, S. Zhao, J. Yu, J. Wang, *Mater. Today Chem.* **2023**, *30*, 101510; b) L. Hu, J. Zhu, C. Duan, J. Zhu, J. Wang, K. Wang, Z. Gu, Z. Xi, J. Hao, Y. Chen, J. Ma, J.-X. Liu, C. Ma, *Cell Rep. Phys. Sci.* **2023**, *4*, 101428.

[19] B. W. Shao, Y. L. Huang, F. D. Han, *Adv. Energy Mater.* **2023**, *13*, 2204098.

[20] S. H. Li, J. Lin, M. Schaller, S. Indris, X. Zhang, T. Brezesinski, C. W. Nan, S. Wang, F. Strauss, *Angew. Chem. Int. Ed.* **2023**, *62*, e202314155.

[21] F. D. Han, A. S. Westover, J. Yue, X. L. Fan, F. Wang, M. F. Chi, D. N. Leonard, N. Dudney, H. Wang, C. S. Wang, *Nat. Energy* **2019**, *4*, 187–196.

[22] P. J. Chandler, E. Lilley, *Phys. Status Solidi A* **1981**, *66*, 183–187.

[23] S. P. Bond, A. Gelder, J. Homer, W. R. Mcwhinnie, M. C. Perry, *J. Mater. Chem. A* **1991**, *1*, 327–330.

[24] L. M. Riegger, R. Schlem, J. Sann, W. G. Zeier, J. Janek, *Angew. Chem. Int. Ed.* **2021**, *60*, 6718–6723.

[25] J. T. Kim, A. Rao, H.-Y. Nie, Y. Hu, W. Li, F. Zhao, S. Deng, X. Hao, J. Fu, J. Luo, H. Duan, C. Wang, C. V. Singh, X. Sun, *Nat. Commun.* **2023**, *14*, 6404.

[26] a) Z. Y. Ning, G. C. Li, D. L. R. Melvin, Y. Chen, J. F. Bu, D. Spencer-Jolly, J. L. Liu, B. K. Hu, X. W. Gao, J. Perera, C. Gong, S. D. D. Pu, S. M. Zhang, B. Y. Liu, G. O. Hartley, A. J. Bodey, R. I. Todd, P. S. Grant, D. E. J. Armstrong, T. J. Marrow, C. W. Monroe, P. G. Bruce, *Nature* **2023**, *618*, 287–293; b) Y. Tang, L. Zhang, J. Chen, H. Sun, T. Yang, Q. Liu, Q. Huang, T. Zhu, J. Huang, *Energy Environ. Sci.* **2021**, *14*, 602–642.

[27] a) L. H. Ye, X. Li, *Nature* **2021**, *593*, 218–222; b) G. V. Alexander, C. Shi, J. O'Neill, E. D. Wachsman, *Nat. Mater.* **2023**, *22*, 1136–1143; c) G. Lu, S. Li, K. Yue, H. Yuan, J. Luo, Y. Liu, Y. Wang, X. Tao, J. Nai, *Battery Energy* **2023**, *2*, 20230044.

[28] a) T. Hakari, A. Hayashi, M. Tatsumisago, *Chem. Lett.* **2015**, *44*, 1664–1666; b) Y. Fujita, T. Hakari, M. Deguchi, Y. Kawasaki, H. Tsukasaki, S. Mori, M. Tatsumisago, A. Sakuda, A. Hayashi, *ACS Appl. Energ. Mater.* **2022**, *5*, 9429–9436.

Manuscript received: October 29, 2023
Accepted manuscript online: January 20, 2024
Version of record online: February 12, 2024